metals

MDPI

Article

Effect of Cold Rolling on Microstructure and Mechanical Properties of a Cast TiNbZr-Based Composite Reinforced with Borides

Maxim Ozerov [1,*], Vitaly Sokolovsky [1], Nikita Yurchenko [1], Ilya Astakhov [1], Elizaveta Povolyaeva [1], Oleg Plekhov [2], Damir Tagirov [1], Nikita Stepanov [1] and Sergey Zherebtsov [1]

[1] Laboratory of Bulk Nanostructured Materials, Belgorod State University, 308015 Belgorod, Russia; sokolovskiy@bsu.edu.ru (V.S.); yurchenko_nikita@bsu.edu.ru (N.Y.); astakhov@bsu.edu.ru (I.A.); povolyaeva@bsu.edu.ru (E.P.); tagirov@bsu.edu.ru (D.T.); stepanov@bsu.edu.ru (N.S.); zherebtsov@bsu.edu.ru (S.Z.)

[2] Institute of Continuous Media Mechanics, Ural Branch of Russian Academy of Science, 614013 Perm, Russia; poa@icmm.ru

* Correspondence: ozerov@bsu.edu.ru; Tel.: +7-4722-58-54-16

Abstract: The TiNbZr/(Ti, Nb)B metal matrix composite with 2.5 vol.% of borides was produced by vacuum arc melting. The composite was then cold-rolled to thickness strains of 10, 20, 50, or 80%. In the initial condition, the composite had a network-like microstructure consisting of the soft TiNbZr matrix (dendrites) and the rigid (Ti, Nb)B shell (interdendritic space). In comparison with the as-cast condition, cold rolling increased strength by 17–35%, depending on the thickness strain. After the maximum thickness strain of 80%, yield strength and ultimate tensile strength of the composite achieved 865 and 1080 MPa, respectively, while total elongation was found to be 5%. Microstructural analysis revealed that cold rolling to 50% resulted in the formation of crossing shear bands caused by the considerable difference in deformation behavior of the matrix and reinforcements. Cold rolling to 80% led to the formation of a lamellar-like microstructure comprising the interlayers of the (Ti, Nb)B phase between the TiNbZr laths. The maximum strain (80% cold rolling) shortened the (Ti, Nb)B fibers into nearly equiaxed particles, with a length to diameter ratio of ~2.

Keywords: medium-entropy alloy; metal matrix composite; boride fibers; cold rolling; deformation; microstructure; mechanical properties

Citation: Ozerov, M.; Sokolovsky, V.; Yurchenko, N.; Astakhov, I.; Povolyaeva, E.; Plekhov, O.; Tagirov, D.; Stepanov, N.; Zherebtsov, S. Effect of Cold Rolling on Microstructure and Mechanical Properties of a Cast TiNbZr-Based Composite Reinforced with Borides. *Metals* **2024**, *14*, 104. https://doi.org/10.3390/met14010104

Academic Editors: Mohammad Jahazi and Zbigniew Pater

Received: 8 November 2023
Revised: 9 January 2024
Accepted: 12 January 2024
Published: 15 January 2024

1. Introduction

To date, stainless steels, titanium, and cobalt alloys have found wide application as metallic biomaterials. Among these options, titanium alloys have the best combination of high specific strength, low density, and good corrosion resistance, which warrant their widespread use in biomedicine [1]. At the same time, the relatively low absolute strength, low hardness, and wear resistance of titanium alloys significantly limit the scope of their application. At the same time, the potential use of titanium alloys as implants for permanent use imposes rather severe restrictions on possible alloying systems, limiting the additions of elements harmful to the human body for creating higher-strength compositions. For example, although the Ti-6Al-4V alloy is still the most widely used orthopedic material, it contains vanadium, which is considered toxic [2], as well as aluminum, which has neurological and genotoxic side effects [3,4]. To provide the required strength without compromising biocompatibility, titanium alloys for medical purposes are alloyed with elements harmless to the human body, such as Nb, Zr, Ta, etc. [5,6], many of which are beta (body-centered cubic; bcc) stabilizers. At the same time, the stabilization of the bcc phase in the alloy by adding a sufficiently large amount of bcc stabilizers not only positively affects the strength properties, it also significantly reduces its elastic modulus, thereby lowering the difference between the elastic moduli of the implant material and the bone. This

factor is extremely important for permanent orthopedic implants, since a large difference between the elastic moduli of the implant material and the bone can lead to incorrect load distribution due to the "stiffness" of the structure, the loosening of the implant, and the need for repeated surgical intervention [7,8].

The medium-entropy equiatomic alloy of the Ti-Nb-Zr system, consisting of the most biocompatible elements, due to the combination of high strength and plastic properties, is a very promising material for use in orthopedic surgery in the form of bone implants [5,9]. This alloy has a significantly lower Young's modulus (48–64 GPa) [5,10], compared to the Ti-6Al-4V alloy (110 GPa), 316L stainless steel (200 GPa), and Co–Cr alloys (210–232 GPa) and is close to the modulus of elasticity of bone tissue (~27 GPa) [11], which is an important factor for its use as a material for implants [12]. In addition, the presence of Zr inhibits the formation of phosphates on the surface of the material, which have a negative effect on the interaction of the implant with the bone tissue [13]. Studies also show a good biocompatibility of the alloys with the Ti-Nb-Zr system [14,15]. Thus, the Ti-Nb-Zr alloy system is undoubtedly one of the best candidates for developing and producing absolutely safe biomedical alloys with highly competitive advantages. However, a wider distribution of these alloys is limited, due to relatively low strength, hardness, and wears resistance [9]. A significant improvement in strength characteristics can be achieved by creating metal matrix composites with high-strength ceramic reinforcing particles [16,17].

One of the most attractive hardening components for pure Ti and titanium alloys is the TiB fiber, which has a good relationship with the titanium matrix, a similar coefficient of thermal expansion with Ti, and good thermal stability [16,17]. The microstructure and mechanical properties of obtained metal matrix composites (MMCs) depend on a number of factors, including the synthesis method (for example, casting or powder metallurgy), parameters of this method, and the volume fraction of embedded borides [16–18]. These issues have been widely studied for titanium-based composites with a hexagonal close-packed (hcp) lattice [18–21] and, to a much lesser extent, for titanium-based composites with a bcc structure [21,22]. For high- and medium-entropy alloys, this issue has been very poorly studied. There is a limited number of known works on the strengthening of Ti-Nb-Zr alloys with borides that show fairly optimistic results [23–26]. Reinforcing a Ti–35Nb–5.7Ta–7.2Zr (at. %) alloy with TiB particles significantly increased the strength, with only minor growth of the elastic modulus of the composite but decreased ductility in comparison with the Ti–35Nb–5.7Ta–7.2Zr alloy [25]. Our recent work [26] showed the positive effect of boride reinforcement on the strength properties of an equiatomic TiNbZr alloy without affecting the biocompatibility.

Another interesting question is the effect of cold deformation on the structure and properties of Ti-Nb-Zr alloy-based composites. Earlier studies have shown a positive effect of thermomechanical treatment (generally conducted at elevated temperatures) on mechanical properties of titanium alloys-based metal matrix composites reinforced by borides [18,20,21]. However, there are no studies on the microstructure evolution of the TiNbZr-based composites during a large cold deformation, while this approach can offer further development of such materials. In this work, the TiNbZr/(Ti, Zr)B composite was subjected to cold rolling to thickness strains of 10–80%; mechanical properties and the microstructure evolution of the composite were thoroughly analyzed.

2. Materials and Methods

Ingots (~60 g weight) of the TiNbZr/(Ti, Nb)B composite with 2.5 vol.% of boride reinforcements were produced in a high-purity argon atmosphere by vacuum arc melting of granules of pure (≥99.9 wt.%) Nb, Ti, Zr, and a powder of TiB_2 (0.7 wt.%) of 99.9% purity.

Specimens measured at 4 × 10 × 20 mm^3 (H × W × L, respectively) were cut out from the as-cast ingots using a Sodick AQ300L electro-discharge machine (Sodick Inc., Schaumburg, IL, USA). Then, the specimens were rolled at room temperature to total thickness strains of 10, 20, 50, and 80%. Unidirectional multipass rolling was performed using a reduction per pass of ~0.25 mm (Figure 1).

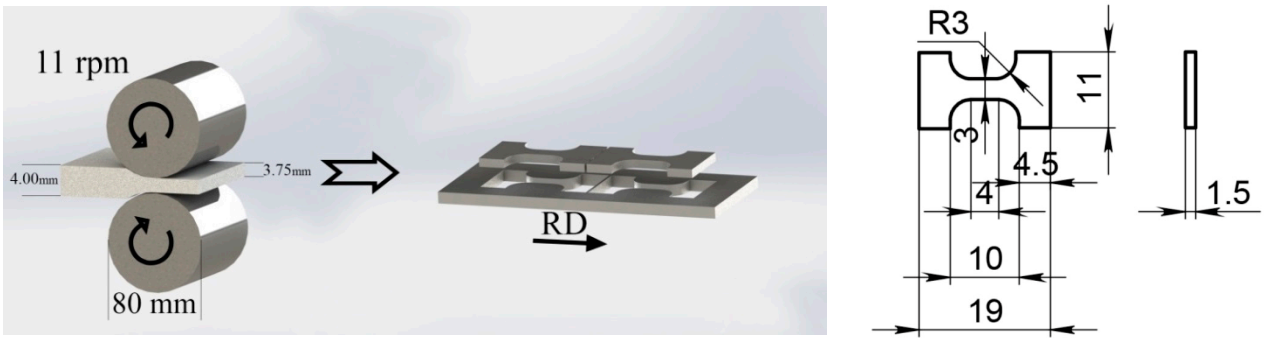

(**a**) (**b**)

Figure 1. Schemes of the rolling procedure (**a**) and tensile specimen (**b**).

Initial and deformed microstructures of the composite were studied using transmission (TEM) and scanning (SEM) electron microscopy. TEM was performed using a JEOL JEM 2100 (JEOL, Tokyo, Japan) microscope operated at 200 kV; the samples for TEM observations were ground to ~100 μm of thickness, and then the thinned foils were subjected to a Struers twin-jet TenuPol-5 (Westlake, OH, USA) in a mixture of 60 mL perchloric acid, 600 mL methanol, and 360 mL butanol at −35 °C and 29.5 V. Selected-area electron diffraction (SAEDs) patterns were used to investigate the composite in the TEM examination via the Digimizer ver. 4.3.0 software (MedCalc Software Ltd., Ostend, Belgium). The specimens for SEM were prepared by careful mechanical polishing; etching was performed using the Kroll's reagent (95% H_2O, 3% HNO_3, 2% HF). SEM investigations were performed using a FEI Quanta 600 FEG microscope (Thermo Fisher Scientific, Hillsboro, OR, USA) operated at 30 kV. The linear intercept method was used to estimate the average length and diameter of the boride fibers. The Digimizer ver. 4.3.0 software was used to carry out these measurements. For EBSD analysis, the final surfaces of the samples under study were obtained by 24 h vibratory polishing with a colloidal silica suspension. EBSD investigations were carried out using the TSL OIM Analysis ver. 7.3.1 software (EDAX Corporation, Mahwah, NJ, USA). The EBSD maps were obtained using a scan step size of 0.2 μm.

Tensile tests were carried out on an Instron 5882 machine (Instron, Canton, OH, USA) at room temperature with an initial strain rate of 10^{-3} s^{-1}. Dog-bone-shaped tensile specimens with a gauge of 4 × 3 × 1.5 mm^3 (L × W × H, respectively) (Figure 1) were cut from the ingots/plates using a Sodick AQ300L (Sodick Inc., Schaumburg, IL, USA) wire electrical discharge machine and carefully mechanically polished before testing; two samples were tested for each condition. The resonance frequency damping analysis (RFDA) method was applied for the Young's modulus determination. The value of the Young's modulus was measured to be 78.5 GPa for the composite. This value was used when constructing the tensile flow curves.

3. Results

3.1. Initial Microstructure

In the initial as-cast condition (Figure 2a), the composite consisted of a continuous phase (matrix), with a chemical composition close to an equatomic TiNbZr, and multiple (Ti, Nb)B fibers (in accordance with [26]). The (Ti, Nb)B fibers had a volume fraction of 2.5% and a transverse size of ~400 nm, as confirmed by the etched surface images (Figure 2b). EBSD analysis showed a rather homogeneous distribution of (Ti, Nb)B fibers as clusters (due to the small diameter of the fibers, these areas are mainly presented by dots with a low confidence index (CI) and are therefore seen in black on the EBSD map) or discontinuous arrays, mainly along boundaries of large (~500 μm) bcc matrix grains (Figure 2c), resembling a core-shell structure. Further TEM studies showed that the (Ti, Nb)B fibers had a prismatic cross-section [27]. The interphase boundary between the bcc

matrix and the (Ti, Nb)B fibers was clear, without any transition zone; defects like cracks, pores, or delamination were not observed (Figure 2d).

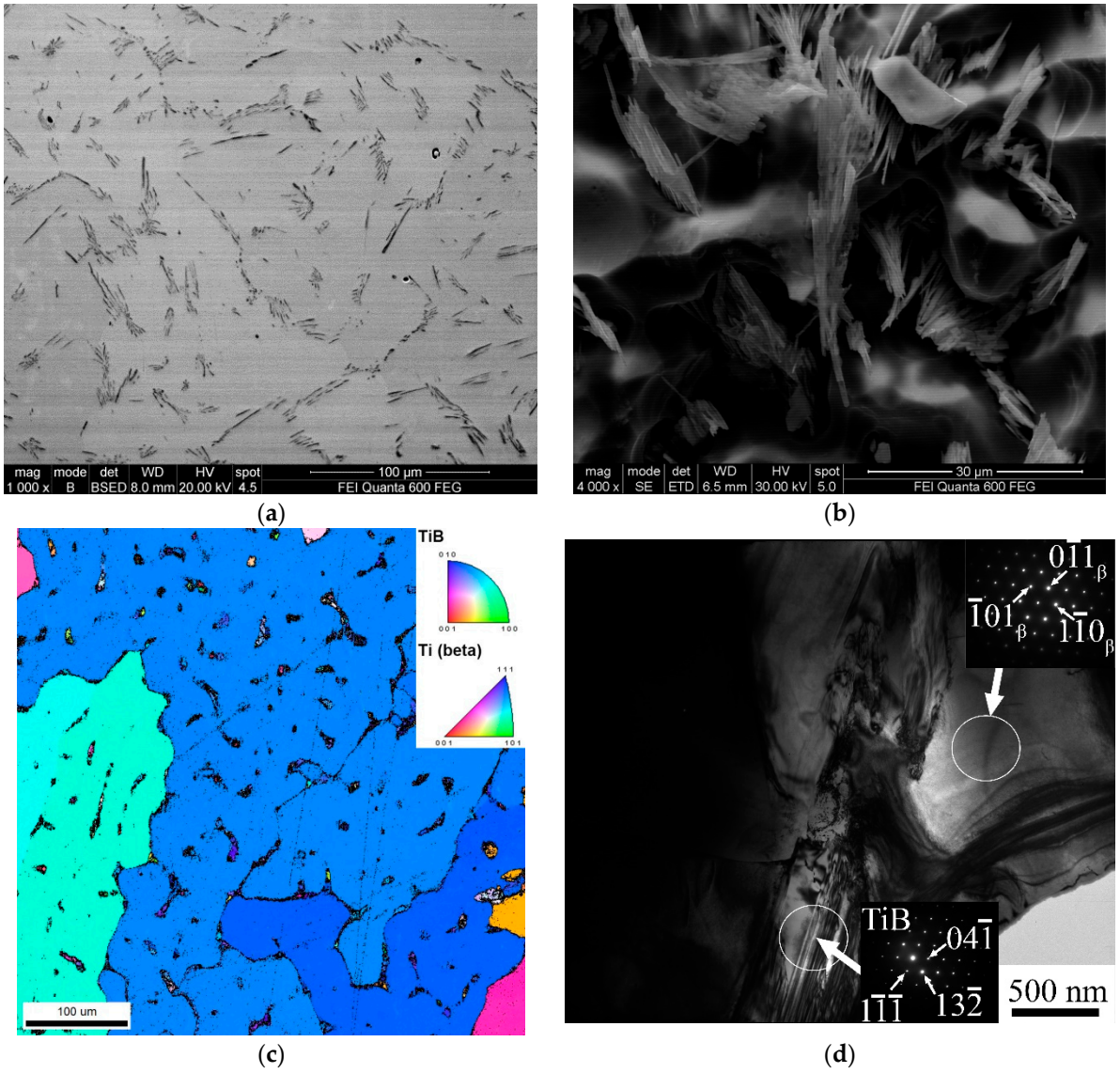

Figure 2. Initial microstructures of the composite; (**a**,**b**) SEM images, © EBSD IPF map, and (**d**) TEM image. (**a**,**c**) Polished surfaces, and the (**b**) etched surface. Dots with a CI (confidence index) < 0.1 were excluded from the consideration on the EBSD map (**c**). Note the greater magnification in (**d**). Please note that the photographs were taken using different types of microscopies.

3.2. Mechanical Properties during Cold Rolling

The mechanical behavior of the TiNbZr/(Ti, Nb)B composite was evaluated under tension in the as-cast state and after cold rolling (CR) to 10, 20, 50, and 80% of the thickness strain (Figure 2; Table 1). The as-cast alloy showed yield strength and ultimate tensile strengths of 720 and 800 MPa, respectively. The deformation curve of the as-cast alloy contained a short strain-hardening stage (uniform elongation ~4%) with further strain localization and some decrease in flow stress, resulting in a total elongation of 10% (Figure 2).

Table 1. Room temperature mechanical properties in tension for the as-cast and cold-rolled specimens of the TiNbZr/(Ti, Nb)B composite.

Condition	Yield Strength, MPa	Ultimate Tensile Strength, MPa	Elongation, %
As-cast	720 ± 5	800 ± 7	10 ± 0.5
CR 10%	730 ± 8	800 ± 8	3 ± 0.3
CR 20%	830 ± 9	880 ± 10	1 ± 0.2
CR 50%	850 ± 8	-	0.3 ± 0.05
CR 80%	865 ± 12	1080 ± 15	5 ± 0.4

CR altered the mechanical properties and deformation behavior in quite a complex manner. CR to 10% led to only a minor strength increment, while it made the alloy much less ductile (Figure 3, Table 1). Further rolling resulted in an increase in strength, decreasing ductility to almost zero at 50% CR. Surprisingly, after CR to a maximum thickness strain of 80%, the alloy attained both the highest yield strength (865 MPa) and the ultimate tensile strength (1080 MPa), and it showed an increase in elongation, compared to less-deformed counterparts. Its deformation behavior was also different. After passing the yield point, the 80% CR alloy demonstrated the strongest and most prolonged strain stage amid both the as-cast and deformed states studied.

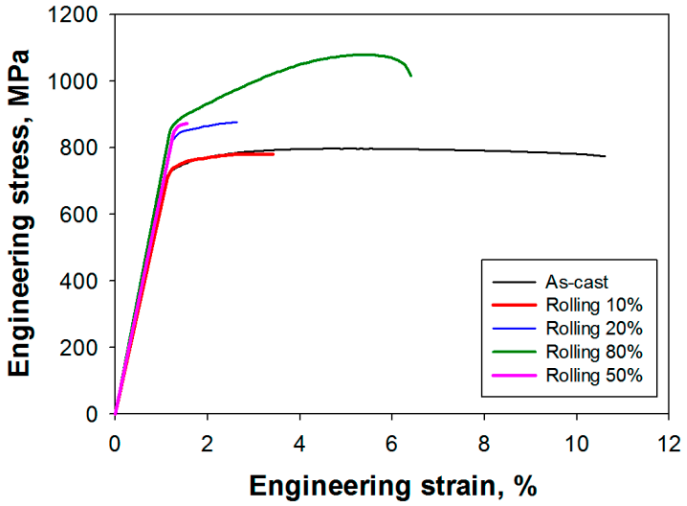

Figure 3. Tensile flow curves obtained at 20 °C of the as-cast and rolled specimens of the composite.

3.3. Microstructure Evolution during Cold Rolling

The microstructure of the composite after CR to 10 or 20% experienced minor changes in comparison with the as-cast state (Figure 4a). CR to 50% flattened the soft TiNbZr matrix areas, while the (Ti, Nb)B shell elongated towards the metal flow direction (Figure 4b). However, the eutectic structure of the (Ti, Nb)B colonies can still be recognized. Further CR to 80% resulted in the formation of a lamellar microstructure. The (Ti, Nb)B phase network was found to be broken, transforming into separate interlayers between the TiNbZr laths. The (Ti, Nb)B phase interlayers often had complex geometry with pronounced variations in thickness (in a range of 5–50 μm (Figure 4c)); the degradation of the eutectic (Ti, Nb)B structure that was often associated with the shear bands formation in the bcc matrix was noted. At the etched surface, a considerable shortening of (Ti, Nb)B fibers in the shear bands can be seen (Figure 4d).

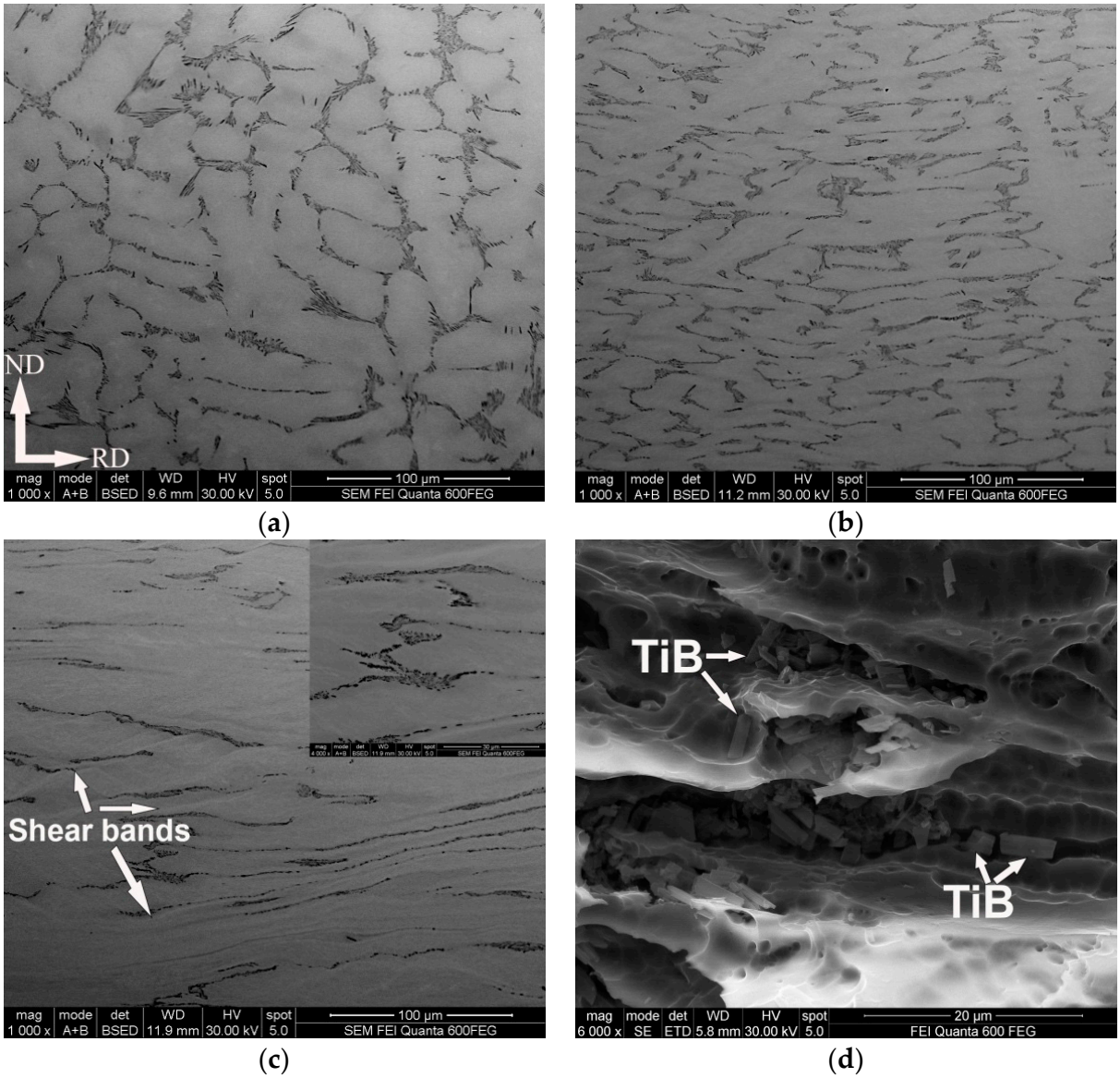

Figure 4. SEM images of polished (**a**–**c**) or etched surfaces (**d**) of the composite taken after rolling to thickness strains of 20% (**a**), 50% (**b**), and 80% (**c**,**d**). Note the greater magnification in (**d**).

Indeed, CR was associated with a decrease in the apparent length of the (Ti, Nb)B fibers from ~18 µm in the initial condition to ~1 µm after 80% (Figure 5). Since the cross-section of the fibers was ~400 nm, the length-to-diameter ratio reached the value of ~2, suggesting the transformation of (Ti, Nb)B fibers into rather equiaxed particles at the final stage of CR. The shortening of the fibers occurred quite evenly, and the whole dependence can be approximated by a nearly straight line.

EBSD and kernel average misorientation (KAM) maps of the composite after CR to 10, 20, 50, and 80% are shown in Figure 5. CR to 10% did not result in notable changes in the IPF map of the composite (Figure 6a). However, KAM maps (a measure of local grain misorientation; generally, the KAM value is high in deformed grains, due to the higher density of geometrically necessary (GNDs) dislocations [28]) showed some increase in the density of the GNDs nearby boundaries of the bcc grains (Figure 6b; see also the quality map of this area in Supplementary Materials).

After 20% of CR, the grain structure of the composite can still be recognized; however, short shear bands (with lengths of 30–200 µm) dividing the microstructure onto separate fragments were also observed (Figure 6c). The EBSD maps imply the overlapping of the

nucleating shear bands and the existing interdendrite boundaries (seen as the widening of severely deformed areas with low CI), thereby suggesting the preferable formation of shear bands near the (Ti, Nb)B shell. The misorientation of these fragments only slightly changed with respect to the "parent's" grains. The KAM map expectably showed a considerable local increase in the strain in (and close to) the shear bands (Figure 6d). Further CR to 50% resulted in the development of shear deformation, and the formation of a network consisting of crossed shear bands mainly declined ~45° from the rolling plane (Figure 6e). Although the shear bands reflect an inclination of the material to strain localization, the distribution of the shear bands in the microstructure was quite homogeneous at this stage. However, during further deformation to 80% of thickness reduction, the microstructure clearly divided to heavily deformed regions (which often comprised the remnants of (Ti, Nb)B shell), alternating with areas that were almost not involved in plastic flow (Figure 6f). The KAM maps of the most deformed conditions clearly showed high-density GNDs in the shear bands and along the remnants of the (Ti, Nb)B shell (Figure 6f,h).

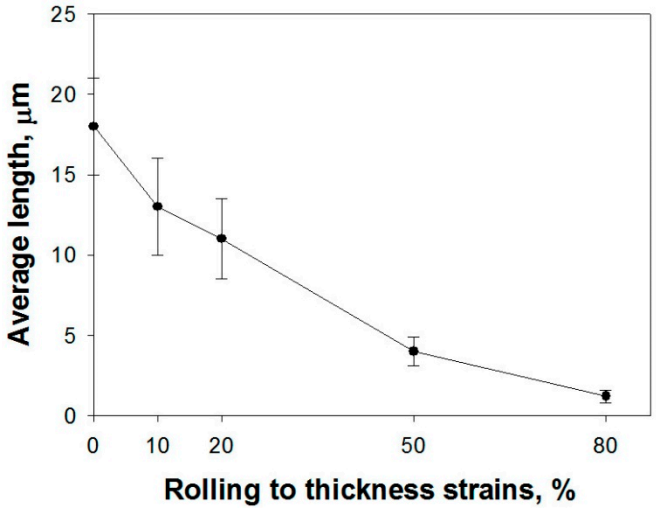

Figure 5. Apparent lengths of the (Ti, Nb)B fibers in the composite as a function of the strain during CR.

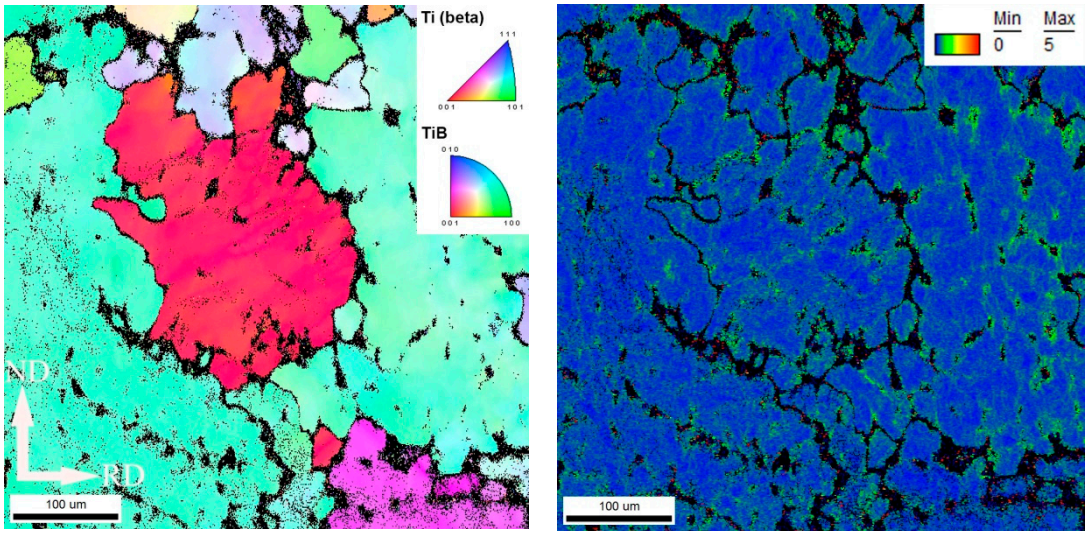

(**a**) (**b**)

Figure 6. *Cont.*

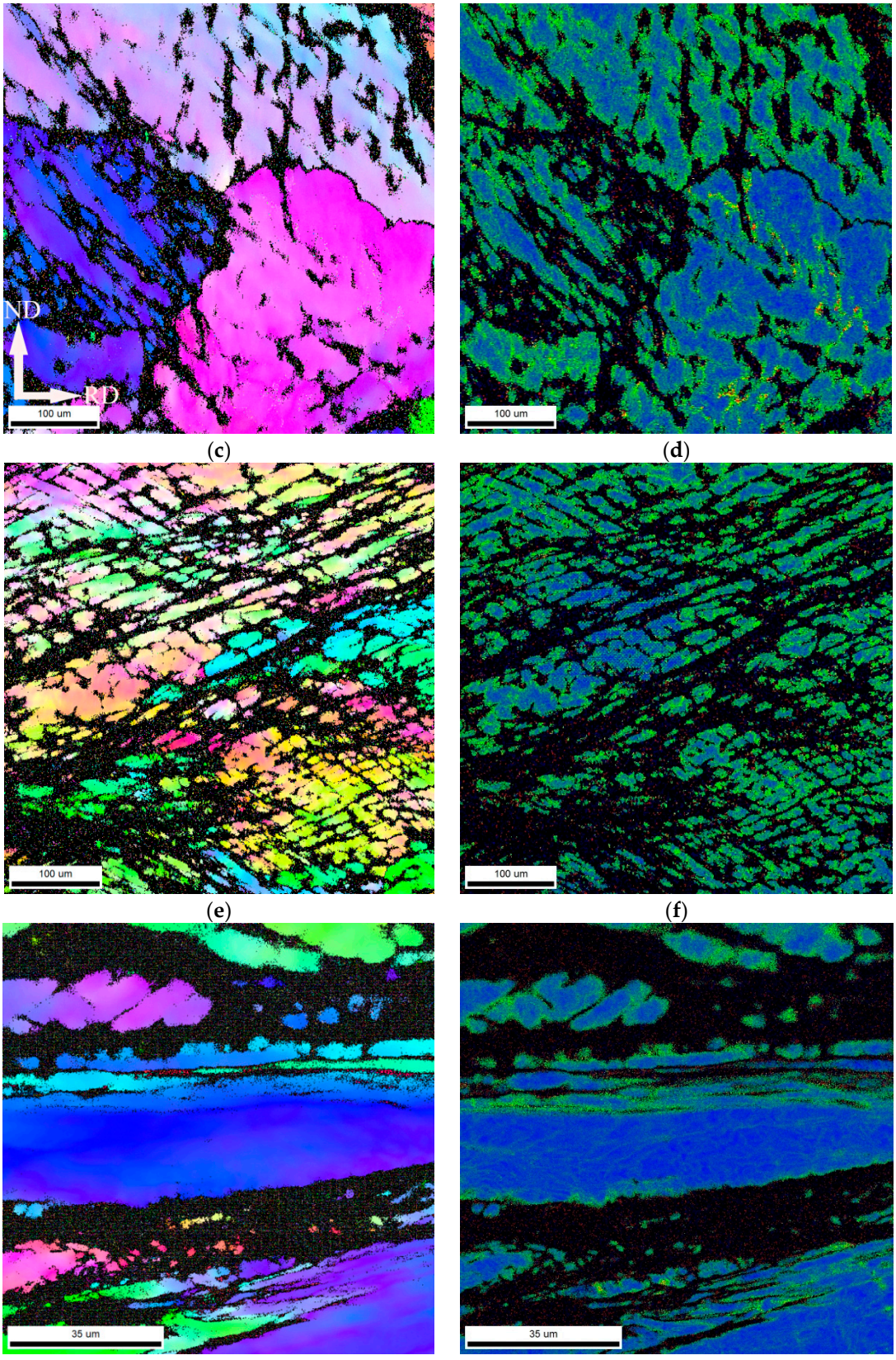

(**c**) (**d**)

(**e**) (**f**)

(**g**) (**h**)

Figure 6. EBSD IPF (**a**–**c**) and KAM (**d**) maps taken from the TD plane of the TiNbZr/(Ti, Nb)B composite cold-rolled to thickness strains of 10% (**a**,**b**), 20% (**c**,**d**), 50% (**e**,**f**), and 80% (**g**,**h**). Dots with a CI (confidence index) < 0.1 were excluded from the consideration. Note the greater magnifications in (**g**,**h**).

TEM analysis demonstrated a considerable difference between areas either apart from or within the shear bands (Figure 7). In the former case, the microstructure comprised dislocation arrays alternating with the area with a relatively low dislocation density (Figure 7a). Boundaries between the (Ti, Nb)B particles and the TiNbZr matrix were still well recognized and did not contain excessive amounts of dislocations. In the area of the more intensive shear deformation, a lamellar structure was formed with high dislocation density (Figure 7b). The width of the lamellae was found to be ~200 nm. The microstructure in the shear bands also comprised the bcc phase only (Figure 7c).

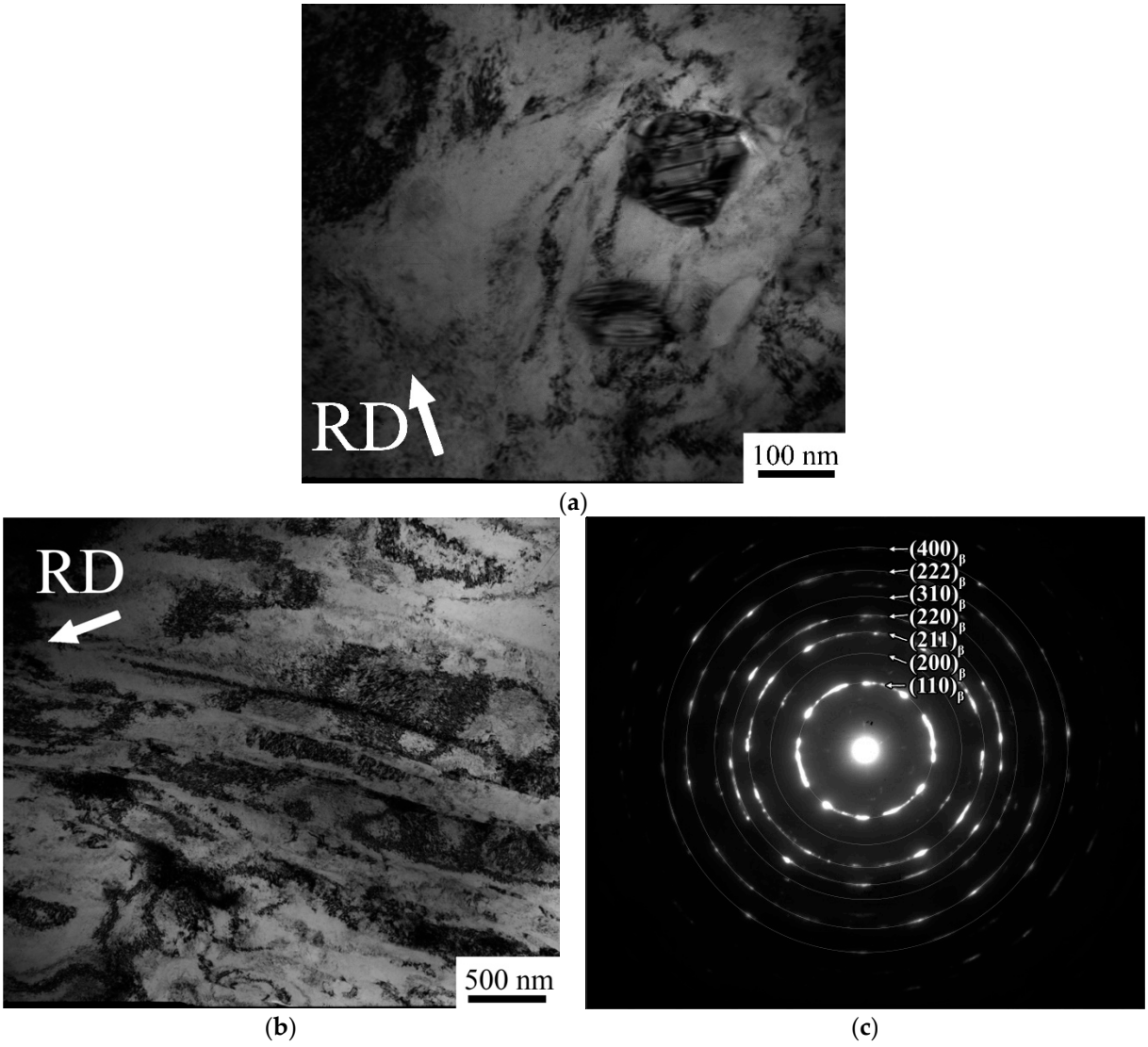

Figure 7. TEM images of the TiNbZr/(Ti, Nb)B composite cold-rolled to thickness strains of 50% (**a**) and 80% (**b**,**c**) of the thickness reduction.

4. Discussion

One of the most interesting points was the formation of a network-like structure in the cast composite. Based on earlier results [26], the present composite with 2.5 vol.% of (Ti, Nb)B formed from the liquid state via the hypoeutectic reaction (eutectic point for the Ti-based alloys, and boron is expected at 6.5–8 vol% of TiB [29,30]). The SEM image (Figure 2a) and image quality map (Supplementary Materials, Figure S1) suggested the formation during crystallization of a dendritic structure in which the core region was the primary TiNbZr phase, while (Ti, Nb)B formed as a eutectic phase in the interdendritic spaces. The formation of the network-like structure in Ti-based composites reinforced with TiB whiskers

was obtained using powder metallurgy viz. low-energy milling of titanium alloys and TiB_2 powders and further hot isostatic pressing [21]. Recent results have shown that the network distribution (in contrast to the conventional homogeneous one) can improve both the strength and tensile ductility of the metal matrix composites [17,21]. The strengthening effect could be attributed to a rigid TiB network, while ductility could be provided by a soft matrix. Indeed, in our case, in the initial as-cast condition, the composite with 2.5 vol.% of the reinforcements possessed quite a good tensile ductility of 10% for MMCs [31].

Meanwhile, the obtained results demonstrate the possibility of deforming TiNbZr/(Ti, Nb)B metal matrix composites with 2.5 vol.% of boride reinforcements under very large strain at room temperature without the formation of any surface defects or intermediate annealing. CR resulted in a noticeable increase in strength by 17–35%, in comparison with the as-cast condition. (It should be noted also that the addition of 2.5 vol.% of (Ti, Nb)B reinforcements into the TiNbZr resulted itself in a ~20% increase in strength [26,31,32]) (Figure 3, Table 1). The observed increase in strength can be associated with several reasons. One of the obvious results of large deformation (i.e., CR to 80%) is the increased dislocation density and the formation of a dislocation substructure, due to which the strength of the composite can increase considerably. Another factor that can contribute to strength is associated with the shortening of the (Ti, Nb)B fibers. Normally, the contribution of "elongated" particles (i.e., those with a length-to-diameter ratio $l/d > 40$ [33]) to strength is related to the load transfer from the softer and more ductile metallic matrix to the stiff and strong ceramic reinforcements (load transfer mechanism) [34]. Shortening of the (Ti, Nb)B fibers during CR to $l/d \approx 2$ activates the Orowan strengthening mechanism. In turn, the Orowan mechanism can offer a much greater contribution to strength, in comparison to that of the load transfer mechanism [33]. Other strengthening factors may be associated with crystallographic and metallographic (preferable orientation of the remnants of the (Ti, Nb)B shell along the metal flow direction) textures.

However, if an increase in strength during CR was an anticipated result, some increase in ductility after 80% of CR (in comparison with the lower rolling strains) (Figure 3) appeared more surprising. This phenomenon was obviously associated with features of the microstructure of the composite under the initial condition (Figure 8a) and during CR. At the first stages of deformation, an increase in dislocation density (Figure 8b) was accompanied by an increase in strength and a decrease in ductility to 1% after 20% of thickness reduction (Table 1). From the "conventional" point of view, this result is associated with a much lower ability of the deformed matrix to accommodate deformation during the tensile test.

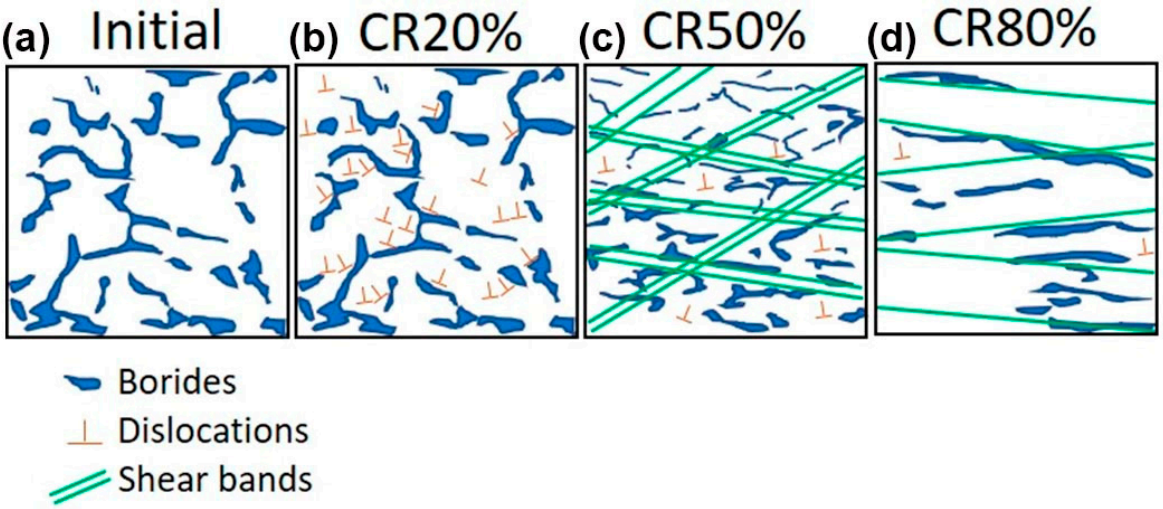

Figure 8. Schematic representations of microstructure evolution of the TiNbZr/(Ti, Nb)B composite during CR.

CR to 50% of thickness reduction considerably changed the microstructure, due to the formation of another network comprised of shear bands (Figures 8c and S2). Shear bands broke the network created by (Ti, Nb)B and made the composite stronger but almost brittle (total elongation ~0.3%, Table 1). The formation of the shear bands network can be caused by a pronounced difference in the deformation behavior between the matrix and the reinforcements. For example, the results of the crystal plasticity finite element simulation reported for various heterophase microstructures [35], as well as earlier experimental results [36–38], clearly showed that the co-deformation of such structures can often proceed via pronounced shear banding induced by stress concentration at the interfaces. Similar processes can be developed along the TiNbZr/(Ti, Nb)B interfaces, resulting in the formation of shear bands. The (Ti, Nb)B particles were involved in shear straining, due to which the gradual shortening of the fibers to a nearly equiaxed form was observed (Figure 5). It is worth noting that in non-reinforced TiNbZr, the character of dislocation distribution during deformation is much more homogeneous without the formation of obvious shear bands [32].

Further straining to 80% CR resulted in the formation of the lamellar microstructure. The network of shear bands (as well as the network of (Ti, Nb)B) was transformed into hard layers alternating with almost undeformed (Figure 6h) and relatively soft layers of TiNbZr. The formation of such undeformed areas can hardly be related to recrystallization/recovery processes but was rather caused by a specific redistribution of the soft matrix, due to the extrusion of the soft matrix from between the remnants of the (Ti, Nb)B shell. The presence of these areas, which are able to accumulate dislocations during tension, and the combination of the strengthening factors described above resulted in a balance of high strength (ultimate tensile strength of 1080 MPa) and reasonable ductility (total elongation of 5%).

The presence of soft TiNbZr matrix areas can be confirmed by fractographic analysis. In the cold-rolled to 80% specimen, the fraction of areas that showed typical ductile fracture (Figure 9) attained ~30%. Meanwhile, the fracture surfaces of the specimens rolled to 10, 20, and 50% represented mainly typical brittle fractures, with cleavage facets and river patterns (Figure 9).

Therefore, the obtained results showed the capability of deformation treatment of the metal matrix composite reinforced by short fibers for attaining a desirable strength/ductility combination. However, further studies in this direction are needed to establish the anisotropy of such materials and the effects of heat treatment on the structure and properties of the cold-rolled materials.

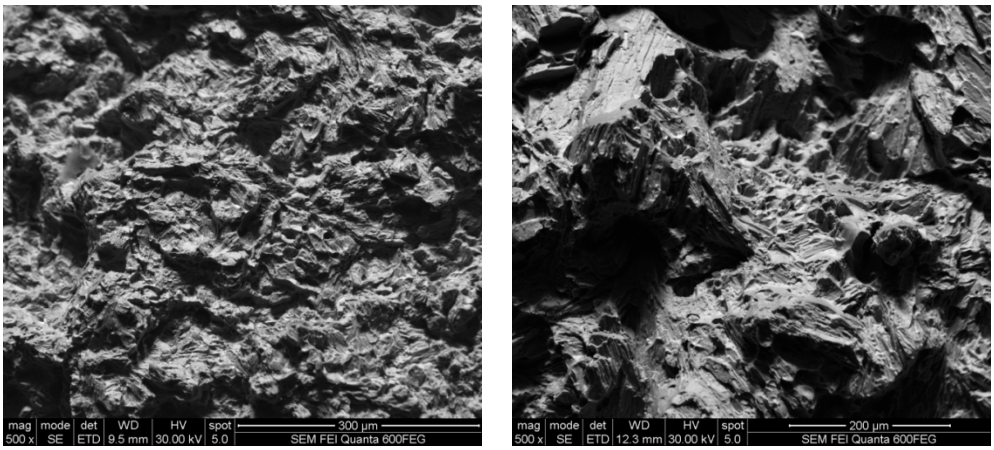

(**a**) (**b**)

Figure 9. *Cont.*

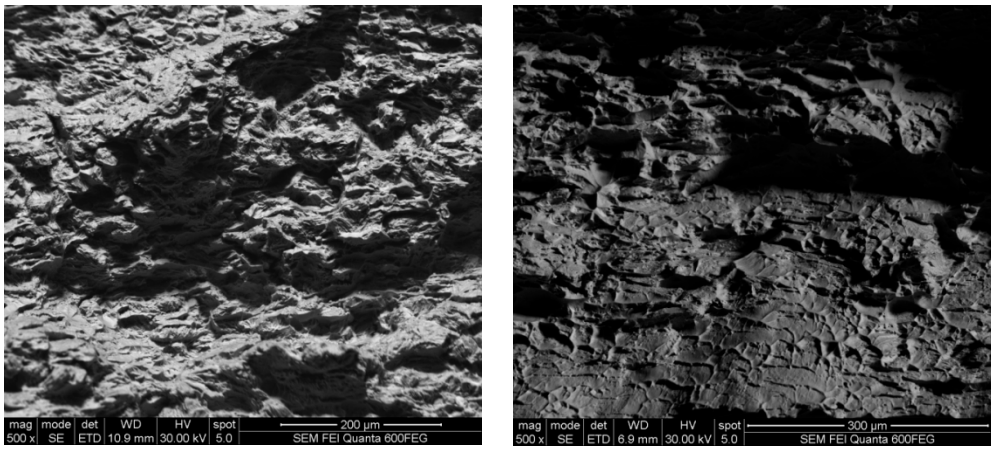

(**c**) (**d**)

Figure 9. Fracture surfaces of tensile specimens after cold rolling to 10% (**a**), 20% (**b**), 50% (**c**), and 80% (**d**).

5. Conclusions

The cast specimens of the TiNbZr/(Ti, Zr)B composite were subjected to cold rolling to thickness strains of 10–80%; the following conclusions were drawn based on the obtained results:

1. In the initial as-cast condition, the alloy had a network-like structure consisting of areas of the TiNbZr matrix (~500 µm size) surrounded by arrays of (Ti, Nb)B fibers. The (Ti, Nb)B fibers had a volume fraction of 2.5% and a transverse size of ~400 nm.
2. Cold rolling resulted in a noticeable increase in strength by 17–35% in comparison with the as-cast condition. Deformation to a thickness strain of 80% led to growths in yield strength and ultimate tensile strength of the composite from 720 to 865 MPa and from 800 to 1080 MPa, respectively. Ductility of the alloy decreased from 10% in the as-cast condition to 0.3% after 50% CR; however further straining resulted in an increase in ductility to 5% after 80% of CR.
3. The microstructure of the composite after CR to 10 or 20% of thickness reduction did not change noticeably in comparison with the as-cast condition. Rolling to 50% resulted in the development of shear deformation, and the formation of a network consisting of crossing shear bands declined mainly ~45° from the rolling plane. Further deformation until 80% of thickness reduction resulted in the formation of a lamellar-like microstructure, in which the refined (Ti, Nb)B layers separated the TiNbZr laths. After deformation to 80%, the TiB fibers of practically equiaxed particles, with a length to diameter ratio of ~2, were transformed.

Supplementary Materials: The following supporting information can be downloaded at: https://www.mdpi.com/article/10.3390/met14010104/s1, Figure S1: Image quality maps taken form the TD plane of the TiNbZr/(Ti, Nb)B composite cold rolled to a thickness strain of 10% (a), 20% (b), 50% (c) and 80% (d); Figure S2: SEM images of polished (a–h) or etched surfaces (i–l) of the composite taken after rolling to thick-ness strains 10% (a,b,i), 20 % (c,d,j), 50 % (e,f,k) and 80 (g,h,l).

Author Contributions: Conceptualization, S.Z. and N.S.; methodology, M.O., N.Y., V.S., I.A., O.P. and E.P.; validation, S.Z. and M.O.; formal analysis, S.Z., N.Y. and M.O.; investigation, M.O., N.Y., E.P., D.T., I.A. and V.S.; resources, S.Z. and O.P.; data curation, S.Z., M.O. and D.T.; writing—original draft preparation, M.O.; writing—review and editing, S.Z., N.S. and N.Y.; visualization, M.O. and V.S.; supervision, S.Z. and M.O.; project administration, S.Z.; funding acquisition, S.Z. All authors have read and agreed to the published version of the manuscript.

Funding: This research was funded by the Russian Science Foundation, Grant Number N° 22-19-00476.

Data Availability Statement: The raw/processed data required to reproduce these findings cannot be shared at this time as the data also form part of an ongoing study.

Acknowledgments: The authors gratefully acknowledge the financial support from the Russian Science Foundation (Grant Number N° 22-19-00476). The authors are grateful to the personnel of the Joint Research Centre, Belgorod State University for their assistance with the instrumental analysis. Casting of the composites was carried out under financial support from the programs for the creation and development of the world-class scientific center "Supersound" for 2020–2025 with the financial support of the Ministry of Education and Science of Russia (Agreement N° 075-15-2022-329 dated 21 April).

Conflicts of Interest: The authors declare no conflicts of interest.

References

1. Zhang, L.C.; Chen, L.Y. A Review on Biomedical Titanium Alloys: Recent Progress and Prospect. *Adv. Eng. Mater.* **2019**, *21*, 1801215. [CrossRef]
2. Okazaki, Y. A new Ti-15Zr-4Nb-4Ta alloy for medical applications. *Curr. Opin. Solid State Mater. Sci.* **2001**, *5*, 45–53. [CrossRef]
3. Flaten, T.P. Aluminium as a risk factor in Alzheimer's disease, with emphasis on drinking water. *Brain Res. Bull.* **2001**, *55*, 187–196. [CrossRef]
4. Lima, P.D.; Vasconcellos, M.C.; Montenegro, R.C.; Bahia, M.O.; Costa, E.T.; Antunes, L.M. Genotoxic effects of aluminum, iron and manganese in human cells and experimental systems: A review of the literature. *Hum. Exp. Toxicol.* **2011**, *30*, 1435–1444. [CrossRef] [PubMed]
5. Ozan, S.; Lin, J.; Li, Y.; Ipek, R.; Wen, C. Development of Ti–Nb–Zr alloys with high elastic admissible strain for temporary orthopedic devices. *Acta Biomater.* **2015**, *20*, 176–187. [CrossRef]
6. Laheurte, P.; Prima, F.; Eberhardt, A.; Gloriant, T.; Wary, M.; Patoor, E. Mechanical properties of low modulus β titanium alloys designed from the electronic approach. *J. Mech. Behav. Biomed. Mater.* **2010**, *3*, 565–573. [CrossRef]
7. Black, J. *Biological Performance of Materials, Fundamentals of Biocompatibility*; CRC Taylor & Francis: Boca Raton, FL, USA, 2006.
8. Huiskes, R.; Weinans, H.; Vanrietbergen, B. The relationship between stress shielding and bone-resorption around total hip stems and the effects of flexible materials. *Clin. Orthop. Relat. Res.* **1992**, *274*, 124–134. [CrossRef]
9. Senkov, O.N.; Rao, S.; Chaput, K.J.; Woodward, C. Compositional effect on microstructure and properties of NbTiZr-based complex concentrated alloys. *Acta Mater.* **2018**, *151*, 201–215. [CrossRef]
10. Meng, Q.; Guo, S.; Liu, Q.; Hu, L.; Zhao, X. A β-type TiNbZr alloy with low modulus and high strength for biomedical applications. *Prog. Nat. Sci. Mater. Int.* **2014**, *24*, 157–162. [CrossRef]
11. Rho, J.Y.; Tsui, T.Y.; Pharr, G.M. Elastic properties of human cortical and trabecular lamellar bone measured by nanoindentation. *Biomaterials* **1997**, *18*, 1325–1330. [CrossRef]
12. Geetha, M.; Singh, A.K.; Asokamani, R.; Gogia, A.K. Ti based biomaterials, the ultimate choice for orthopaedic implants—A review. *Prog. Mater. Sci.* **2009**, *54*, 397–425. [CrossRef]
13. Hanawa, T.; Hiromoto, S.; Asami, K.; Okuno, O.; Asaoka, K. Surface oxide films on titanium alloys regenerated in Hanks' solution. *Mater. Trans.* **2002**, *43*, 3000–3004. [CrossRef]
14. Mishchenko, O.; Ovchynnykov, O.; Kapustian, O.; Pogorielov, M. New Zr-Ti-Nb Alloy for Medical Application: Development, Chemical and Mechanical Properties, and Biocompatibility. *Materials* **2020**, *13*, 1306. [CrossRef]
15. Aguilar Maya, A.E.; Grana, D.R.; Hazarabedian, A.; Kokubu, G.A.; Luppo, M.I.; Vigna, G. Zr–Ti–Nb porous alloys for biomedical application. *Mater. Sci. Eng. C* **2012**, *32*, 321–329. [CrossRef]
16. Hayat, M.D.; Singh, H.; He, Z.; Cao, P. Titanium metal matrix composites: An overview. *Compos. Part A Appl. Sci. Manuf.* **2019**, *121*, 418–438. [CrossRef]
17. Shetty, R.; Hegde, A.; Shetty SV, U.K.; Nayak, R.; Naik, N.; Nayak, M. Processing and Mechanical Characterisation of Titanium Metal Matrix Composites: A Literature Review. *J. Compos. Sci.* **2022**, *6*, 388. [CrossRef]
18. Morsi, K. Review: Titanium–titanium boride composites. *J. Mater. Sci.* **2019**, *54*, 6753–6771. [CrossRef]
19. Ozerov, M.; Klimova, M.; Kolesnikov, A.; Stepanov, N.; Zherebtsov, S. Deformation behavior and microstructure evolution of a Ti/TiB metal-matrix composite during high-temperature compression tests. *Mater. Des.* **2016**, *112*, 17–26. [CrossRef]
20. Ozerov, M.; Klimova, M.; Sokolovsky, V.; Stepanov, N.; Popov, A.; Boldin, M.; Zherebtsov, S. Evolution of microstructure and mechanical properties of Ti/TiB metal-matrix composite during isothermal multiaxial forging. *J. Alloys Compd.* **2019**, *770*, 840–848. [CrossRef]
21. Huang, L.; An, Q.; Geng, L.; Wang, S.; Jiang, S.; Cui, X.; Zhang, R.; Sun, F.; Jiao, Y.; Chen, X.; et al. Multiscale Architecture and Superior High-Temperature Performance of Discontinuously Reinforced Titanium Matrix Composites. *Adv. Mater.* **2021**, *33*, 2000688. [CrossRef]
22. Zherebtsov, S.; Ozerov, M.; Klimova, M.; Moskovskikh, D.; Stepanov, N.; Salishchev, G. Mechanical behavior and microstructure evolution of a Ti-15Mo/TiB titanium–matrix composite during hot deformation. *Metals* **2019**, *9*, 1175. [CrossRef]
23. Samuel, S.; Nag, S.; Scharf, T.W.; Banerjee, R. Wear resistance of laser-deposited boride reinforced Ti-Nb-Zr-Ta alloy composites for orthopedic implants. *Mater. Sci. Eng. C* **2008**, *28*, 414–420. [CrossRef]
24. Nag, S.; Samuel, S.; Puthucode, A.; Banerjee, R. Characterization of novel borides in Ti-Nb-Zr-Ta + 2B metal-matrix composites. *Mater. Charact.* **2009**, *60*, 106–113. [CrossRef]

25. Majumdar, P.; Singh, S.B.; Dhara, S.; Chakraborty, M. Influence of in situ TiB reinforcements and role of heat treatment on mechanical properties and biocompatibility of β Ti-alloys. *J. Mech. Behav. Biomed. Mater.* **2012**, *10*, 1–12. [CrossRef]
26. Ozerov, M.; Sokolovsky, V.; Nadezhdin, S.; Zubareva, E.; Zherebtsova, N.; Stepanov, N.; Huang, L.; Zherebtsov, S. Microstructure and mechanical properties of medium-entropy TiNbZr alloy-based composites, reinforced with boride particles. *J. Alloys Compd.* **2023**, *938*, 168512. [CrossRef]
27. Feng, H.; Zhou, Y.; Jia, D.; Meng, Q.; Rao, J. Growth mechanism of in situ TiB whiskers in spark plasma sintered TiB/Ti metal matrix composites. *Cryst. Growth Des.* **2006**, *6*, 1626–1630. [CrossRef]
28. Calcagnotto, M.; Ponge, D.; Demir, E.; Raabe, D. Orientation gradients and geometrically necessary dislocations in ultrafine grained dual-phase steels studied by 2D and 3D EBSD. *Mater. Sci. Eng. A* **2010**, *527*, 2738–2746. [CrossRef]
29. Ivasishin, O.M.; Teliovych, R.V.; Ivanchenko, V.G.; Tamirisakandala, S.; Miracle, D.B. Processing, Microstructure, Texture, and Tensile Properties of the Ti-6Al-4V-1.55B Eutectic Alloy. *Metall. Mater. Trans. A* **2008**, *39*, 402–416. [CrossRef]
30. Gaisin, A.; Imayev, V.M.; Imayev, R.M. Effect of hot forging on microstructure and mechanical properties of near α titanium alloy/TiB composites produced by casting. *J. Alloys Compd.* **2017**, *723*, 385–394. [CrossRef]
31. Ozerov, M.; Sokolovsky, V.; Stepanov, N.; Zherebtsov, S. Microstructure and tensile properties of TiNbZr alloy-based metal-matrix composites, reinforced with borides. *AIP Conf. Proc.* **2023**, *2899*, 020109.
32. Eleti, R.R.; Stepanov, N.; Yurchenko, N.; Zherebtsov, S.; Maresca, F. Cross-kink unpinning controls the medium- to high-temperature strength of body-centered cubic NbTiZr medium-entropy alloy. *Scr. Mater.* **2022**, *209*, 114367. [CrossRef]
33. Chen, B.; Shen, J.; Ye, X.; Jia, L.; Li, S.; Umeda, J.; Takahashi, M.; Kondoh, K. Length effect of carbon nanotubes on the strengthening mechanisms in metal matrix composites. *Acta Mater.* **2017**, *140*, 317–325. [CrossRef]
34. Maurya, P.; Kota, T.; Gibmeier, J.; Wanner, A.; Roy, S. Review on study of internal load transfer in metal matrix composites using diffraction techniques. *Mater. Sci. Eng. A* **2022**, *840*, 142973. [CrossRef]
35. Jia, N.; Roters, F.; Eisenlohr, P.; Raabe, D.; Zhao, X. Simulation of shear banding in heterophase co-deformation: Example of plane strain compressed Cu–Ag and Cu–Nb metal matrix composites. *Acta Mater.* **2013**, *61*, 4591–4606. [CrossRef]
36. Sauvage, X.; Renaud, L.; Deconihout, B.; Blavette, D.; Ping, D.H.; Hono, K. Solid state amorphization in cold drawn Cu/Nb wires. *Acta Mater.* **2001**, *49*, 389–394. [CrossRef]
37. Ohsaki, S.; Kato, S.; Tsuji, N.; Ohkubo, T.; Hono, K. Bulk mechanical alloying of Cu–Ag and Cu/Zr two-phase microstructures by accumulative roll-bonding process. *Acta Mater.* **2007**, *55*, 2885–2895. [CrossRef]
38. Raabe, D.; Mattissen, D. Microstructure and mechanical properties of a cast and wire-drawn ternary Cu–Ag–Nb in situ composite. *Acta Mater.* **1998**, *46*, 5973–5984. [CrossRef]